

Local intraspecific aggregation in phytoplankton model communities: spatial scales of occurrence and implications for coexistence

Coralie Picoche¹, William R. Young², Frédéric Barraquand¹

¹Institute of Mathematics of Bordeaux, University of Bordeaux and CNRS, Talence, France

²Scripps Institution of Oceanography, La Jolla, California, USA

Abstract

The coexistence of multiple phytoplankton species despite their reliance on similar resources is often explained with mean-field models assuming mixed populations. In reality, observations of phytoplankton indicate spatial aggregation at all scales, including at the scale of a few individuals. Local spatial aggregation can hinder competitive exclusion since individuals then interact mostly with other individuals of their own species, rather than competitors from different species. To evaluate how microscale spatial aggregation might explain phytoplankton diversity maintenance, an individual-based, multispecific representation of cells in a hydrodynamic environment is required. We formulate a three-dimensional and multi-specific individual-based model of phytoplankton population dynamics at the Kolmogorov scale. The model is studied through both simulations and the derivation of spatial moment equations, in connection with point process theory. The spatial moment equations show a good match between theory and simulations. We parameterized the model based on phytoplankters' ecological and physical characteristics, for both large and small phytoplankton. Defining a zone of potential interactions as the overlap between nutrient depletion volumes, we show that local species composition—within the range of possible interactions—depends on the size class of phytoplankton. In large phytoplankton, individuals are surrounded by cells from other species, while in small phytoplankton, individuals remain in mostly monospecific clusters. Spatial structure therefore favours intra- over inter-specific interactions for small phytoplankton, which likely contributes to coexistence mechanisms. Other factors behind diversity maintenance must be examined for large phytoplankton.

Keywords: aggregation; coexistence; individual-based model; phytoplankton; spatial moment equations; spatial point process

*corresponding authors: coralie.picoche@u-bordeaux.fr & frederic.barraquand@u-bordeaux.fr

Introduction

Phytoplankton communities are among the most important photosynthetic groups on Earth, being at the bottom of the marine food chain, and responsible for approximately half the global primary production (Field *et al.*, 1998). Their contribution to ecosystem functions is only matched by their contribution to biodiversity. Indeed, phytoplankton communities are characterized by a surprisingly high biodiversity. For example, a single sample as small as a few mL can contain up to seventy species (REPHY, 2017; Widdicombe & Harbour, 2021). This observation is usually called the “paradox of the plankton” (Hutchinson, 1961), which refers to the conflict between the observed diversity of species competing for similar resources in a seemingly homogeneous environment, and models predicting that only a few species will persist by outcompeting the others (MacArthur & Levins, 1964; Huisman & Weissing, 1999; Schippers *et al.*, 2001). Phytoplankton models for coexistence are now almost as diverse as their model organisms (Record *et al.*, 2014), but they often describe only a handful of species, which does not correspond to the diversity observed in the field. When modeling rich communities (> 10 species), classical answers to the plankton paradox involving temporal fluctuations (e.g., Li & Chesson, 2016; Chesson, 2018) are not always sufficient to maintain a realistic diversity. For instance, we found that a phytoplankton community dynamics model with environmental fluctuations and storage effect still requires extra niche differentiation for coexistence, which manifests in stronger intraspecific than interspecific interactions (Picoche & Barraquand, 2019). However, it is not clear that we should resort to hidden niches to explain phytoplankton coexistence, as most models also make hidden simplifying assumptions that could be relaxed. One that we relax here is mean-field dynamics at the microscale. Indeed, field observations have revealed phytoplankton patchiness for more than a century (Bainbridge, 1957; Stocker, 2012), from the macro- to the micro-scale (Leonard *et al.*, 2001; Doubell *et al.*, 2006; Font-Muñoz *et al.*, 2017).

Phytoplankton patchiness can at least be partly explained by the hydrodynamics of their environment: the size of these organisms is mostly below the size of the smallest eddy (i.e., the Kolmogorov scale). In a typical aquatic environment such as the ocean, phytoplankton individuals are embedded in viscous micro-structures (Peters & Marrasé, 2000) while phytoplankton populations are displaced by a turbulent flow at slightly larger scales (Martin, 2003; Prairie *et al.*, 2012). Phytoplankton organisms therefore live in an environment where fluid viscosity dominates at the scale of an individual but turbulent dispersion dominates on length scales characteristic of a small population of those individuals (Estrada *et al.*, 1987; Prairie *et al.*, 2012).

This leads us to consider demography in the context of this environmental variation created by hydrodynamics processes. Individual-based models provide a convenient depiction of population dynamics and movement at the microscale (Hellweger & Bucci, 2009). In this framework, population growth is a result of individual births and deaths. Aggregation of particles can emerge from local reproduction coupled with limited dispersal, which can happen in a fluid where turbulence and diffusion are not strong enough to disperse kin aggregates (Young *et al.*, 2001). The resulting aggregation can affect the dynamics of the populations at the community level: even when

interactions are identical between individuals of the same species (conspecifics) or between individuals of different species (heterospecifics), the combination of local reproduction and same-scale high dispersal limitation and strong interactions leads to stronger intraspecific interactions than interspecific interactions at the population level, which is a major stabilizing mechanism (Detto & Muller-Landau, 2016). Indeed, a high intra-to-interspecific interaction strength ratio makes a species control its abundance more than it controls the abundance of other species, which is associated with coexistence in theoretical models (Levine & HilleRisLambers, 2009; Barabás *et al.*, 2017) and often observed in the field at the population level (Adler *et al.*, 2018; Picoche & Barraquand, 2020). Therefore, the microscale spatial distribution of individuals likely affects the interaction structure within a community, and may sustain diversity.

Existing models of phytoplankton populations near the Kolmogorov scale — between 1 mm and 1 cm in an oceanic environment (Barton *et al.*, 2014) — focus on a single species and the clustering of its individuals (Young *et al.*, 2001; Birch & Young, 2006; Bouderbala *et al.*, 2018; Breier *et al.*, 2018). They share similarities to dynamic point process models (Law *et al.*, 2003; Bolker & Pacala, 1999; Plank & Law, 2015) developed initially with larger organisms in mind. When phytoplankton individual-based models consider multiple types of organisms, they focus for now on how organisms with opposite characteristics (e.g., increase versus decrease in density with turbulence in Borgnino *et al.*, 2019; Arrieta *et al.*, 2020) segregate spatially, or on coexistence for species that have contrasted trait values (e.g., size in Benczik *et al.*, 2006). This is useful as an explanation of how species with marked differences might coexist. The difficulty of the coexistence problem, however, is that we have to explain how closely related species or genera (e.g., within diatoms), many of whom have similar size, buoyancy, chemical composition, etc., manage to coexist within a single trophic level. This requires modelling *similar* species in a spatially realistic environment and objectively quantifying whether they aggregate or segregate in space.

To do so, we build a multispecific version of the Brownian Bug Model (BBM) of Young *et al.* (2001), an individual-based model which includes a chaotic advection process mimicking a turbulent fluid flow, passive diffusion of organisms, as well as stochastic birth and death processes. The initial version of this model (Young *et al.*, 2001) coupled limited dispersal and local reproduction with ocean-like microscale hydrodynamics, and showed spatial clusters of individuals of the same species. The original BBM was limited to a single species and was illustrated with two-dimensional simulations. The model was not strongly quantitative (Picoche *et al.*, 2022) in the sense that parameters were not informed by current knowledge on phytoplankton biology (numbers of cells per liter, diffusion characteristics, etc.). As phytoplankton organisms live in a three-dimensional environment, informing the model with more realistic parameters required us to shift to three dimensions. We also extend the model to multiple species, and consider two size classes for our phytoplankton communities, which are either made of nanophytoplankton (3 μm diameter, $\approx 10^6$ cells/L) or microphytoplankton (50 μm , $\approx 10^4$ cells/L). We populate each community with 3 to 10 different species.

The Brownian Bug model (in its original single-species form as in the multispecies version considered here) is

linked to spatial branching processes. Without advection, it combines a continuous-time, discrete-state model for population growth and a continuous-time, continuous-space Brownian motion for particle diffusion (Birch & Young, 2006). It is further complexified by a turbulent flow in Young *et al.* (2001); Picoche *et al.* (2022) as well as here. In spite of this complexity, it remains possible to derive the dynamics of pair density functions, which quantify the degree of intra- and interspecific clustering of organisms, via correlations between positions of organisms (see Methods). Thus we can understand emergent spatial structure in analytic details and compare these predictions with the results from three-dimensional simulations. Furthermore, because we do not consider direct interactions between organisms, the multispecies spatial point process that represents the stable state of the BBM is a random superposition of spatial point processes for each species (Illian *et al.*, 2008). This enables us to derive, in addition to pair correlation functions, analytical formulas for the species composition of the neighbourhood of an individual, which are more readily ecologically interpreted than pair density or correlation functions.

Model and spatial statistics

Brownian Bug Model

The Brownian Bug Model (BBM) describes the dynamics of individuals in a turbulent and viscous environment, including demographic processes. The model is continuous in space and time. Here we extend the mostly two-dimensional, monospecific version in Young *et al.* (2001), to three dimensions and S species.

Each individual is characterized by its species i and its position $\mathbf{x}^T = (x, y, z)$. The population dynamics are modeled by a linear birth-death process with birth rate λ_i and death rate μ_i . Each individual independently follows a Brownian motion with diffusivity D_i , and is advected by a common stochastic flow modeling the turbulence with Lyapunov exponent γ (also called the stretching parameter). This means that the separation $s(t)$ between two individuals k and l increases with time as $\ln(|\mathbf{x}_k - \mathbf{x}_l|(t)) \propto \gamma t$.

Within a given community (the set of all individuals of the S species), all species share the same parameters: λ_i , μ_i and D_i values can change between communities, as we later consider small and large phytoplankton, but are set to common values within a community. On the contrary, γ describes the environment and is not community-specific, i.e., all individuals are displaced similarly by turbulent stirring. For numerical simulations, time needs to be discretized (this is required for diffusion and advection modelling). The approximated model advances through time in steps of duration of τ . During each interval, events unroll as follow:

1. demography: each individual can either reproduce with probability $p_i = \lambda_i \tau$ (forming a new individual of the same species i at the same position \mathbf{x} as the parent), die with probability $q_i = \mu_i \tau$, or remain unchanged with probability $1 - p_i - q_i$.
2. diffusion: each individual moves to a new position $\mathbf{x}(t + t') = \mathbf{x}(t) + \delta \mathbf{x}(t)$. The random displacement $\delta \mathbf{x}(t)$

is drawn from a Gaussian distribution $\mathcal{N}(0, \Delta_i)$ with $D_i = \frac{\Delta_i^2}{2\tau}$ the diffusivity.

3. turbulence: each individual is displaced by a turbulent flow, following the Pierrehumbert map (Pierrehumbert, 1994), adapted in its three-dimension version (Ngan & Vanneste, 2011), which writes

$$\begin{aligned} x(t + \tau) &= x(t + t') + U\tau/3 \cos(ky(t + t') + \phi(t)) \\ y(t + \tau) &= y(t + t') + U\tau/3 \cos(kz(t + t') + \theta(t)) \\ z(t + \tau) &= z(t + t') + U\tau/3 \cos(kx(t + \tau) + \psi(t)) \end{aligned} \quad (1)$$

where U is the maximum velocity of the individual, $k = 2\pi/L_s$ is the wavenumber for the flow at the length scale L_s (see below) and $\phi(t)$, $\theta(t)$, $\psi(t)$ are random phases drawn from a uniform distribution between 0 and 2π at the beginning of each time interval, which remain constant during the interval. The shift from continuous to discrete-time turbulence modeling is described in Section S1 in the Supplementary Information. The advection parameter U is related to γ . As the separation between two points grows exponentially with parameter γ due to turbulence, the exponent γ can be estimated as the slope of $1/3 \langle \ln(s(t)) \rangle = f(t)$ in the absence of diffusion and demography.

Individuals are distributed in a cube of side L , with periodic boundary conditions. The cube dimensions are determined to balance computing costs and realistic concentrations of individuals; they represent the accumulation of a few volumes of scale L_s .

Characterization of the spatial distribution

Let W be the observation window (in our case, the whole cube, which we never subsample hereafter). The state of the system at time t can be described as a collection of S populations, where the population of species i is made of n_i individuals randomly distributed in W , with positions $\mathbf{X}_i(t) = [\mathbf{x}_{1,i}(t), \mathbf{x}_{2,i}(t), \dots, \mathbf{x}_{n_i,i}(t)]$. $\mathbf{X}(t) = [\mathbf{X}_1(t), \dots, \mathbf{X}_S(t)]$ arises from a stochastic and spatial individual-based model changing through time, but can also be analyzed as a spatial point process at time t . We note that the point distributions remain the same for all translations $\boldsymbol{\xi}$ (i.e., the point process described by the set $\mathbf{X} = [\mathbf{x}_1, \mathbf{x}_2, \dots, \mathbf{x}_k]$ is the same as $\mathbf{X}_{\boldsymbol{\xi}} = [\mathbf{x}_1 + \boldsymbol{\xi}, \mathbf{x}_2 + \boldsymbol{\xi}, \dots, \mathbf{x}_k + \boldsymbol{\xi}]$): the process is stationary.

One of the useful methods to characterize a spatial point process is through its spatial moments (see examples in Section S2 of the SI). These can be theoretically derived and used to check simulations. The spatial moments of a process are, however, merely statistical indicators which then need to be related to more easily ecologically interpretable quantities. This is the role of the dominance index, which we present below.

Spatial moments

The first-order moment is the intensity of the process, or mean concentration of individuals, whose empirical estimate is $C_i = \frac{\widehat{N_i(W)}}{V(W)}$, where $\widehat{N_i(W)}$ is the empirical number of individuals of species i in the cube W and $V(W) = L^3$

is the volume of the cube; it does not give any information regarding the spatial distribution of individuals, and possibly their spatial correlations.

The second-order product density, or pair density $G(r, t)$, is the expected density of pairs of points separated by a distance r (Law *et al.*, 2003). A similar characteristic can be used for marked spatial point process. In our case, the marks are the species, and we can define $G_{ij}(r, t)$, so that $G_{ij}(r, t)d\mathbf{x}_A d\mathbf{x}_B$ is the probability of finding an individual of species i in volume $d\mathbf{x}_A$ and an individual of species j in volume $d\mathbf{x}_B$, and the distance between the centers of $d\mathbf{x}_A$ and $d\mathbf{x}_B$ is equal to r (pages 219 and 325 in Illian *et al.*, 2008). We show in Picoche *et al.* (2022) that the intraspecific pair density $G_{ii}(r, t)$, in three dimensions, is a solution of

$$\frac{\partial G_{ii}}{\partial t}(r, t) = \frac{2D_i}{r^2} \frac{\partial}{\partial r} \left(r^2 \frac{\partial G_{ii}}{\partial r} \right) + \frac{\gamma}{r^2} \frac{\partial}{\partial r} \left(r^4 \frac{\partial G_{ii}}{\partial r} \right) + 2(\lambda_i - \mu_i)G_{ii} + 2\lambda_i C_i \delta(\mathbf{r}). \quad (2)$$

The pair correlation function $g_{ij}(r, t)$, or pcf, can be derived from the pair density and is defined as

$$g_{ij}(r, t) = \frac{G_{ij}(r, t)}{C_i C_j}. \quad (3)$$

The pcf is equal to one when the spatial distribution of species i individuals is random relative to species j individuals. To compute the intraspecific pcf $g_{ii}(r, t)$ at steady state, considering a population at equilibrium, we integrate Eq. 2 (see Appendices, Eqs. 19-30) with $\lambda_i = \mu_i$ and obtain

$$g_{ii}(r) = 1 + \frac{\lambda_i}{2\pi C_i} \left(\frac{\sqrt{\gamma} \arctan\left(\frac{\sqrt{\gamma} r}{\sqrt{2D_i}}\right)}{2^{3/2} D_i^{3/2}} + \frac{1}{2D_i r} - \frac{\pi \sqrt{\gamma}}{2^{5/2} D_i^{3/2}} \right). \quad (4)$$

The system converges rapidly to the solution in Eq. 4 in the presence of advection. However, when there is no turbulence, convergence is much slower, to the point that an equilibrium assumption would involve unrealistically long timeframes (see Section S3 in the SI). We therefore need a time-dependent formula for the pcf in the absence of advection, which can be obtained in the case where $\gamma = 0$ using a Green's function (see derivation in the Appendices, Eqs. 31-37),

$$g_{ii}(r, t) = 1 + \frac{\lambda_i}{4D_i \pi r C_i} \left\{ 1 - \operatorname{erf} \left(\frac{r}{\sqrt{8D_i t}} \right) \right\}. \quad (5)$$

The above equations match when $\gamma \rightarrow 0$ and $t \rightarrow +\infty$.

As populations of different species do not directly interact, each population is an independent realization of a point process, which means that the distribution of all individuals within the community at time t is a random superposition of stationary point processes and thus $g_{ij}(r, t) = 1$ if $i \neq j$ (Illian *et al.*, 2008, p. 326, eq. 5.3.13).

Related to the pair correlation function is Ripley's K -function $K(r)$. Its marked version, $K_{ij}(r)$, is the average number of points of species j surrounding an individual of species i within a sphere of radius r (Illian *et al.*, 2008),

i.e.,

$$\forall r \geq 0, K_{ij}(r) = \frac{1}{C_j} \mathbb{E}_i (N_j(b(o, r) \setminus \{o\})) \quad (6)$$

where \mathbb{E}_i is the expectation with respect to individuals of species i and $N_j(b(o, r) \setminus \{o\})$ is the number of individuals of species j in the sphere of radius r centred on o , not counting o itself. $K_{ij}(r)$ is related to $g_{ij}(r)$ as

$$g_{ij}(r) = \frac{K'_{ij}(r)}{4\pi r^2}. \quad (7)$$

Combining Eq. 7 and, when $U > 0$, Eq. 4, we can show that (see Appendices, Eqs. 38-44)

$$K_{ii}(r) = \frac{4}{3}\pi r^3 + \frac{2\lambda_i}{C_i} \left(\frac{r^2}{6D_i} + \frac{\sqrt{\gamma} r^3 \arctan(\sqrt{\frac{\gamma}{2D_i}} r)}{6\sqrt{2}D_i^{3/2}} + \frac{\log(\gamma \frac{r^2}{2D_i} + 1)}{6\gamma} - \frac{\sqrt{\gamma}\pi r^3}{12\sqrt{2}D_i\sqrt{D_i}} \right). \quad (8)$$

When $U = 0$, we need a time-dependent solution corresponding to our simulation duration, i.e. (see Appendices, Eq. 46-51)

$$K_{ii}(r, t) = \frac{4}{3}\pi r^3 + \frac{\lambda_i}{C_i D_i} \left(\frac{r^2}{2} - \frac{1}{2} \operatorname{erf}\left(\frac{r}{\sqrt{8D_i t}}\right)(r^2 - 4D_i t) - \frac{\sqrt{2D_i t} r}{\sqrt{\pi}} e^{-r^2/8D_i t} \right). \quad (9)$$

For random superposition of stationary point processes, $K_{ij}(r, t) = \frac{4}{3}\pi r^3$ if $i \neq j$ (Illian *et al.*, 2008, p. 324, eq. 5.3.5).

Dominance index

The dominance index (defined in Table S1 in the Supporting Information of Wiegand *et al.*, 2007) is the ratio between the number of conspecifics and the number of individuals of all species surrounding a given individual.

Let $M_i(r)$ be the average number of individuals within a circle of radius r around an individual of species i , which can also be written with Ripley's K -function as $M_i(r) = C_i K_i(r)$. $M_{ii}(r)$ corresponds to the conspecific neighbourhood and $M_{io}(r)$ corresponds to individuals of all other species. We can then define \mathcal{D}_i as

$$\begin{aligned} \mathcal{D}_i(r) &= \frac{M_{ii}(r)}{M_{ii}(r) + M_{io}(r)} \\ &= \frac{C_i K_{ii}(r)}{\sum_{j=1}^S C_j K_{ij}(r)}. \end{aligned} \quad (10)$$

When individuals of the same species i tend to cluster, $\mathcal{D}_i(r)$ tends to 1 while it tends to the proportion of individuals of species i in the whole community when the distribution is uniform (Section S2 of the SI).

Using Eq. 9 and 10, we obtain the theoretical formula for the dominance index in the presence of advection as

$$\mathcal{D}_i(r) = \frac{C_i \left[\frac{4}{3}\pi r^3 + \frac{\lambda_i}{3C_i D_i} \left(r^2 + \frac{\sqrt{\gamma} r^3 \arctan(\sqrt{\frac{\gamma}{2D_i}} r)}{\sqrt{2}D_i} + \frac{D_i \log(\gamma \frac{r^2}{2D_i} + 1)}{\gamma} - \frac{\sqrt{\gamma}\pi r^3}{2\sqrt{2}D_i} \right) \right]}{\sum_{j=1}^S C_j \left[\frac{4}{3}\pi r^3 + \frac{\lambda_j}{3C_j D_j} \left(r^2 + \frac{\sqrt{\gamma} r^3 \arctan(\sqrt{\frac{\gamma}{2D_j}} r)}{\sqrt{2}D_j} + \frac{D_j \log(\gamma \frac{r^2}{2D_j} + 1)}{\gamma} - \frac{\sqrt{\gamma}\pi r^3}{2\sqrt{2}D_j} \right) \right]}. \quad (11)$$

In the absence of advection ($U = 0, \gamma = 0$), we use the time-dependent dominance index, computed similarly:

$$\mathcal{D}_i(r, t) = \frac{C_i \left[\frac{4}{3}\pi r^3 + \frac{\lambda_i}{C_i D_i} \left(\frac{r^2}{2} - \frac{1}{2} \operatorname{erf}\left(\frac{r}{\sqrt{8D_i t}}\right)(r^2 - 4D_i t) - \frac{\sqrt{2D_i t}}{\sqrt{\pi}} e^{-r^2/8D_i t} \right) \right]}{\sum_{j=1}^S C_j \frac{4}{3}\pi r^3 + \frac{\lambda_j}{D_j} \left(\frac{r^2}{2} - \frac{1}{2} \operatorname{erf}\left(\frac{r}{\sqrt{8D_j t}}\right)(r^2 - 4D_j t) - \frac{\sqrt{2D_j t}}{\sqrt{\pi}} e^{-r^2/8D_j t} \right)}. \quad (12)$$

Parameters

We model two types of organisms: microphytoplankton (defined by a diameter between 20 and 200 μm , here 50 μm) and nanophytoplankton (defined by a diameter between 2 and 20 μm , here 3 μm). These two groups are characterized respectively by a low diffusivity, slow growth and lower concentration vs. high diffusivity, fast growth and higher concentration. Organisms are displaced by a turbulent fluid whose velocity defines the time scale of the discretized model: we give here the reasoning behind parameter values, keeping in mind that our model can only be semi-quantitative. Main parameter definitions and values are given in Table 1.

Advection

We first consider the advection process, due to the turbulence of the environment. We only consider the Batchelor-Kolmogorov regime, i.e the size of the volume W is below the size of the smallest eddy, but above the smallest scale of fluctuations in nutrient concentrations. The defining scale of the environment therefore corresponds to a Reynolds number

$$\text{Re} = \frac{U}{k\nu} \approx 1 \quad (13)$$

where $\nu = 10^{-6} \text{ m}^2 \cdot \text{s}^{-1}$ is the kinematic viscosity for water. The smallest wavenumber k corresponds to the largest length scale L_s (Kolmogorov scale), i.e. $k = 2\pi/L_s$, with $L_s \approx 1 \text{ cm}$ in the ocean (Barton *et al.*, 2014). The definition of the Reynolds number leads to

$$\begin{aligned} 1 &\approx \frac{UL_s}{2\pi\nu} \\ \Leftrightarrow U &\approx \frac{2\pi\nu}{L_s}. \end{aligned} \quad (14)$$

This means that $U = 6.3 \times 10^{-4} \text{ m} \cdot \text{s}^{-1} = 5.4 \times 10^3 \text{ cm} \cdot \text{d}^{-1}$. Using $U\tau/3 = 0.5 \text{ cm}$ as in Young *et al.* (2001), we have $\tau = 2.8 \times 10^{-4} \text{ d} = 24 \text{ s}$. When $U\tau/3 = 0$, i.e. the environment is only diffusive, we keep the same value for τ . For $U\tau/3 = 0.5 \text{ cm}$, $\gamma = 1231 \text{ d}^{-1}$.

Diffusion

If we use the Stokes-Einstein equations (Einstein, 1905, cited from Dusenbery, 2009), diffusivity can be computed with

$$D_i = \frac{RT}{N_A} \frac{1}{6\pi\eta a_i} \quad (15)$$

where $R = 8.314 \text{ J.K}^{-1}.\text{mol}^{-1}$ is the molar gas constant, $T = 293 \text{ K}$ is the temperature, $N_A = 6.0225 \times 10^{23}$ is Avogadro's number, $\eta = 10^{-3} \text{ m}^{-1}.\text{kg.s}^{-1}$ is the dynamic viscosity of water and a_i is the radius of the organism considered.

Using $D_i = \frac{\Delta_i^2}{2\tau}$, we find that

$$\begin{aligned} \Delta_i &= \sqrt{2\tau D_i} \\ \Leftrightarrow \Delta_i &= \sqrt{\frac{RT}{N_A} \frac{\tau}{3\pi\eta a_i}}. \end{aligned} \quad (16)$$

We consider $a_n = 1.5 \text{ }\mu\text{m}$ for nanophytoplankton individuals and $a_m = 25 \text{ }\mu\text{m}$ for microphytoplankton individuals, which allows us to compute Δ_n and Δ_d (see Table 1).

Ecological processes

We study the community at equilibrium, with the birth rate equal to the death rate, i.e. $p_i = q_i \forall i$. We use a microphytoplankton doubling rate of 1 d^{-1} (Bissinger *et al.*, 2008) and consider the fastest-growing nanophytoplankton species, corresponding to a diameter of $3 \text{ }\mu\text{m}$ (Bec *et al.*, 2008), for which the doubling rate is between 2 and 3 d^{-1} (set to 2.5 d^{-1} here).

Parameter	Definition	Value
p_m, q_m	Probability of reproducing/dying for microphytoplankton individuals	2.8×10^{-4}
p_n, q_n	Probability of reproducing/dying for nanophytoplankton individuals	6.9×10^{-4}
U	Turbulent advection speed	$\{0, 0.06\} \text{ cm.s}^{-1}$
Δ_m	Diffusion parameter for microphytoplankton individuals	$6.4 \times 10^{-5} \text{ cm}$
Δ_n	Diffusion parameter for nanophytoplankton individuals	$2.6 \times 10^{-4} \text{ cm}$

Table 1: Definitions and values of the main parameters used in the three-dimension Brownian Bug Model, assuming the duration of a time step τ is 24 seconds.

Range of interaction

As we examine individual aggregation and its potential effects on interactions between species, we have to ascertain the volume in which an individual can be affected by the presence of other individuals, or affects other individuals. We only consider here interactions due to competition for nutrients, and therefore need to define a nutrient depletion volume. We approximate this volume as the sphere of radius r where $C(r) \leq 90\%C_\infty$ with C_∞ the background concentration of the nutrient. The radius of this nutrient depletion volume is maximized when the individual is in stagnant water (diffusion is the only hydrodynamic process). In this case, it corresponds to 10 times the radius of the individual (Jumars *et al.*, 1993; Karp-Boss *et al.*, 1996). We define the maximum distance which allows for potential interactions (due to competition for resources) between two individuals of radius a_i and a_j as $d_{\text{threshold}}$, and the corresponding volume of potential interactions around an organism as $V_{\text{int}} = 4/3\pi d_{\text{threshold}}^3$ with

$$d_{\text{threshold}} = 10a_i + 10a_j. \quad (17)$$

We consider this maximum value as our baseline, keeping in mind that turbulence reduces the size of the nutrient depletion volume and increases the nutrient flux to the cell (Arnott *et al.*, 2021), but determination of the exact shape of the nutrient depletion volume in the presence of turbulence is too complex to be addressed here (Karp-Boss *et al.*, 1996).

We consider a total volume of 1000 cm³ for microphytoplankton and 10 cm³ for nanophytoplankton (volumes are adapted to balance realistic concentrations and computation time) with periodic boundary conditions. Individuals are uniformly distributed in the cube at the beginning of the simulation. We run an idealized simulation with 3 species with an even abundance distribution of about 10⁴ cells/L for microphytoplankton (Picoche & Barraquand, 2020) and 10⁶ cells/L for nanophytoplankton individuals (Edwards, 2019). We then model a more realistic community with 10 species having a skewed abundance distribution (between 55,000 and 400 cells/L for microphytoplankton, according to observations of field abundance distributions in Picoche & Barraquand, 2020, and multiplied by 10² for nanophytoplankton). All simulations are run for 1000 time steps of duration τ . The computation of g and K of simulated distributions is explained in Section S4 of the SI.

Results

We show an example of nanophytoplankton spatial distributions with and without advection at the end of a simulation in Fig. 1: clustering is not visible to the naked eye, even when zooming in the observation volume, in the presence of advection, but removing turbulence helps visualising small aggregates of conspecifics. Microphytoplankton distributions are not so easy to analyse as no clusters can be detected from basic observations, whether advection is included or not (Section S5 of the SI). Statistics are therefore needed to go further in detecting patterns of aggregation.

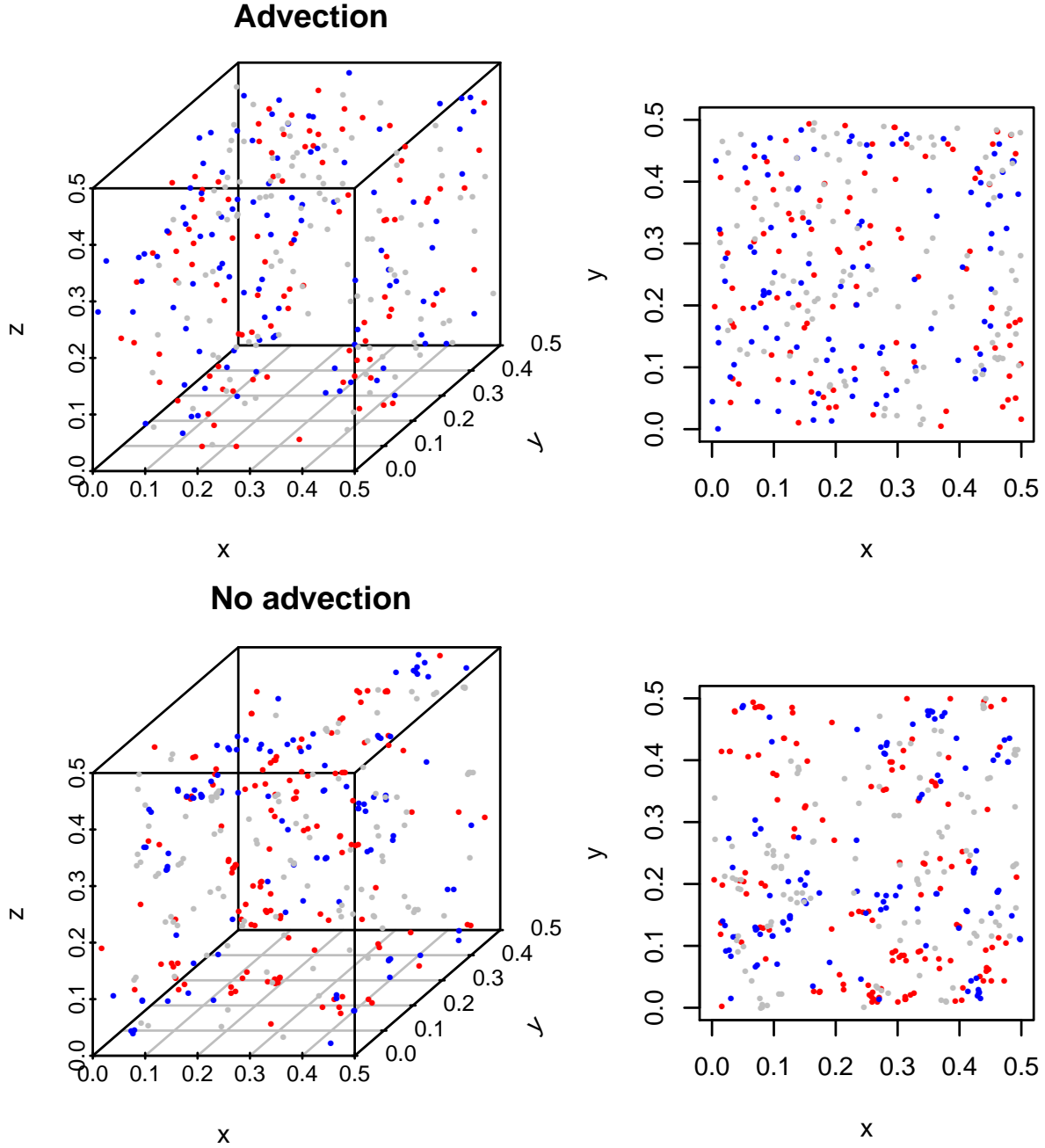


Figure 1: Spatial distributions of a 3-species community of nanophytoplankton with and without advection with density $\lambda = 10^3 \text{ cells.cm}^{-3}$ after 1000 time steps. Each color corresponds to a different species. On the left-hand side, only a zoom on a $0.5 \times 0.5 \times 0.5 \text{ cm}^3$ cube is shown, and its projection on the x-y plane is shown on the right hand-side.

Ripley's K -functions extracted from numerical simulations match theoretical formula (Fig. 2) for both types of organisms, which also indicates that dominance indices extracted from the simulation match theoretical expectations.

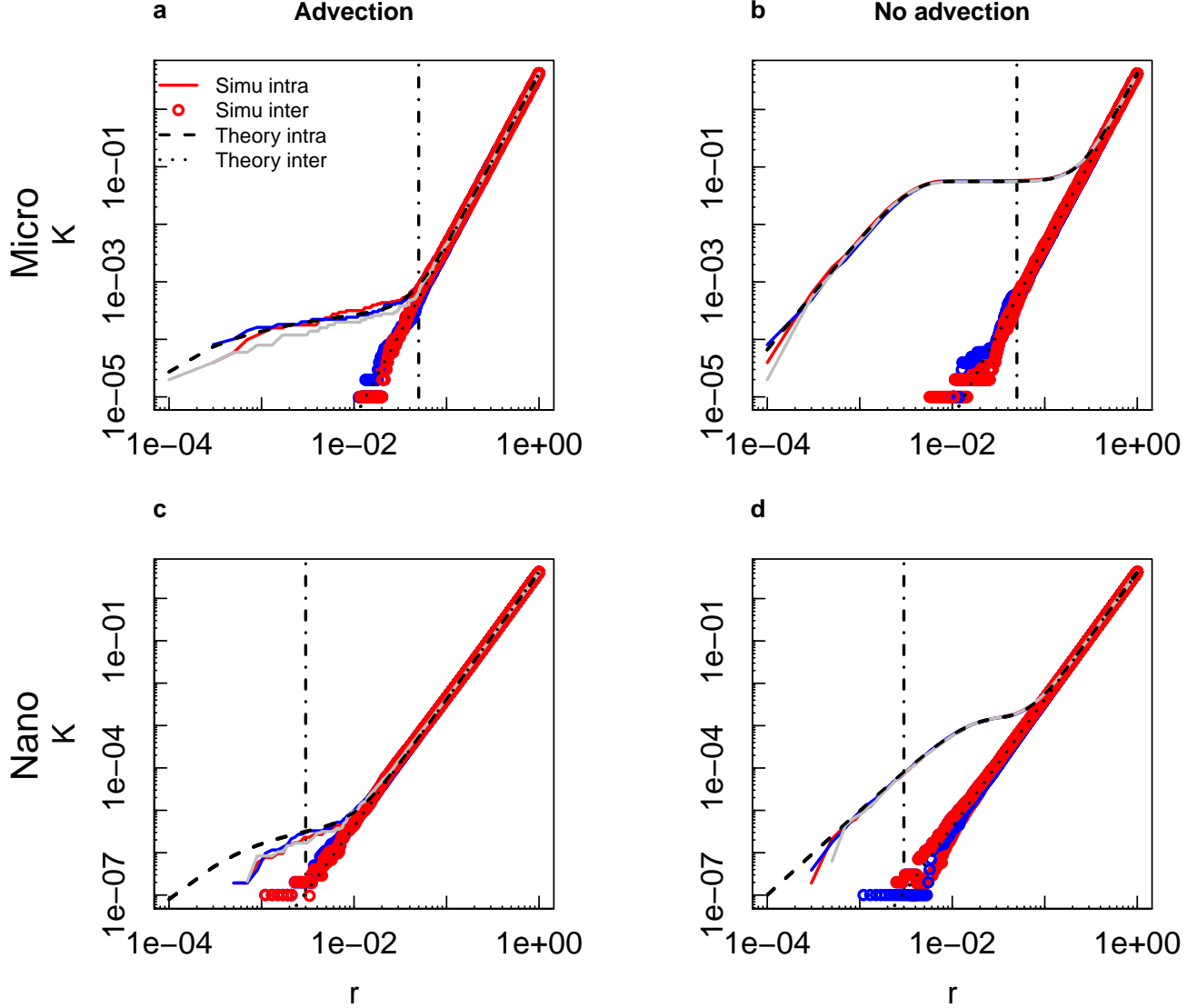


Figure 2: Ripley's K -function as a function of distance (in cm) for microphytoplankton (a-b) and nanophytoplankton (c-d) in a 3-species community with even abundance distributions after 1000 timesteps, with (a, c) and without (b, d) advection. Each color represents a different species. The black dash-dotted line corresponds to the threshold considered as the maximum distance for nutrient-based competition.

Dominance indices all follow a similar pattern (Fig. 3 and 4). The dominance index is close to 1 for small distances: there is always a scale at which an organism is surrounded almost only by conspecifics. The index then decreases sharply to converge at large distances (close to 1 cm) to the proportion of the focus species in the whole community, as it would for a uniform distribution. Patterns differ at intermediate ranges of distances between organisms.

In the presence of advection, the dominance index starts decreasing for a distance between 5 and 10 times lower than when advection is absent, which indicates that organisms are closer to heterospecifics when their environment is turbulent. A quasi-uniform distribution is also reached for smaller distances with advection than without.

Microphytoplankton species start mixing for distances larger than for nanophytoplankton species irrespective of the hydrodynamic regime surrounding them.

In a 3-species community with the same initial abundances, in the presence of advection, microphytoplankton dominance indices are between 0.37 and 0.47 at the distance threshold for potential interactions, while they are between 0.80 and 0.94 for nanophytoplankton species. In the absence of turbulence, dominance indices are all above 0.98 when the distance threshold is reached (Fig. 3). Microphytoplankton organisms are therefore as likely to share their depletion volume with conspecifics as they are with heterospecifics, but only when turbulent advection is accounted for, whereas nanophytoplankton organisms always have almost only conspecifics around them.

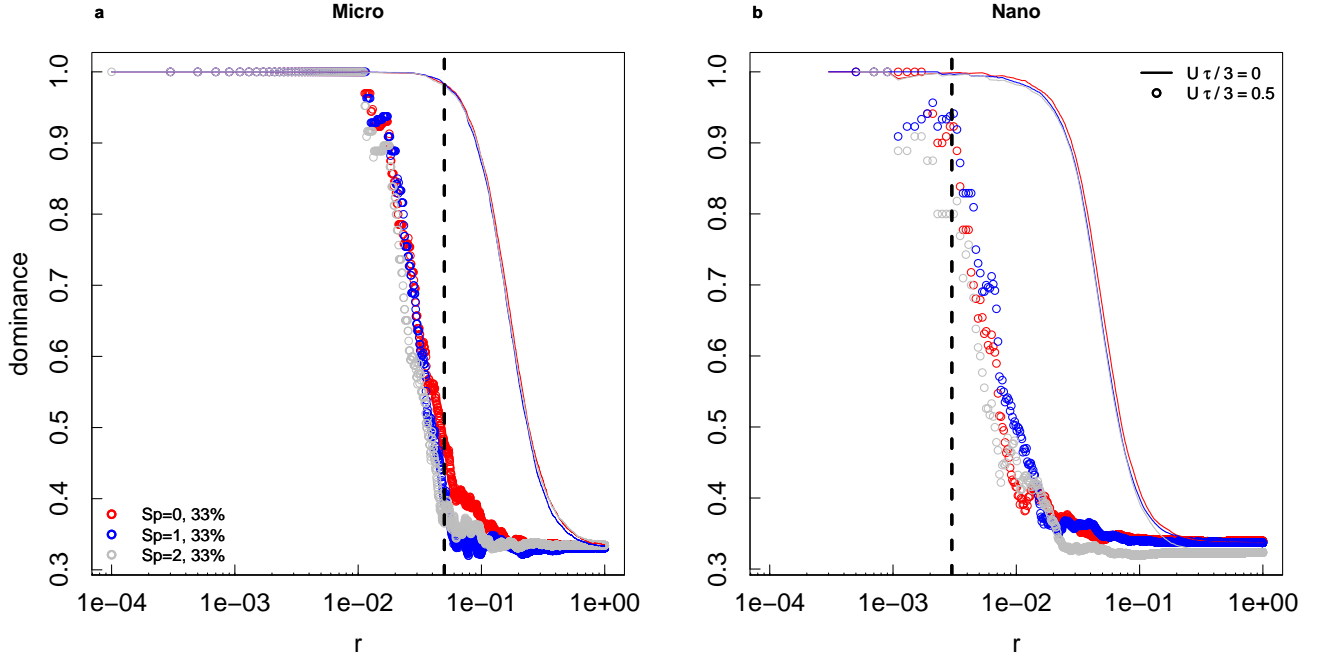


Figure 3: Dominance indices as a function of distance (in cm) for microphytoplankton (a) and nanophytoplankton (b) in a 3-species community with even abundance distributions (final proportions in the community are indicated in the figure) after 1000 timesteps, with (circles) and without (lines) advection. Each color represents a different species. The black dashed line corresponds to the threshold considered as the maximum distance for nutrient-based competition.

These differences between microphytoplankton and nanophytoplankton, and the role of advection, are even more pronounced when considering a 10 species-community with a skewed abundance distribution. (Fig. 4). In the presence of advection, microphytoplankton dominance indices at the distance threshold are between 0.34 (for the most abundant species) and 0.033 (for one of the least abundant species), while they are between 0.90 and 0.85 when advection is not taken into account. Nanophytoplankton species, too, are more mixed: dominance indices vary between 0.54 and 0.2 when the depletion threshold is reached (with an exception of 0 for one particular species which had no conspecific for radii below 10^{-2} cm) when organisms are displaced by turbulence, while the same quantity is between 1 and 0.97 when they are only subject to diffusion.

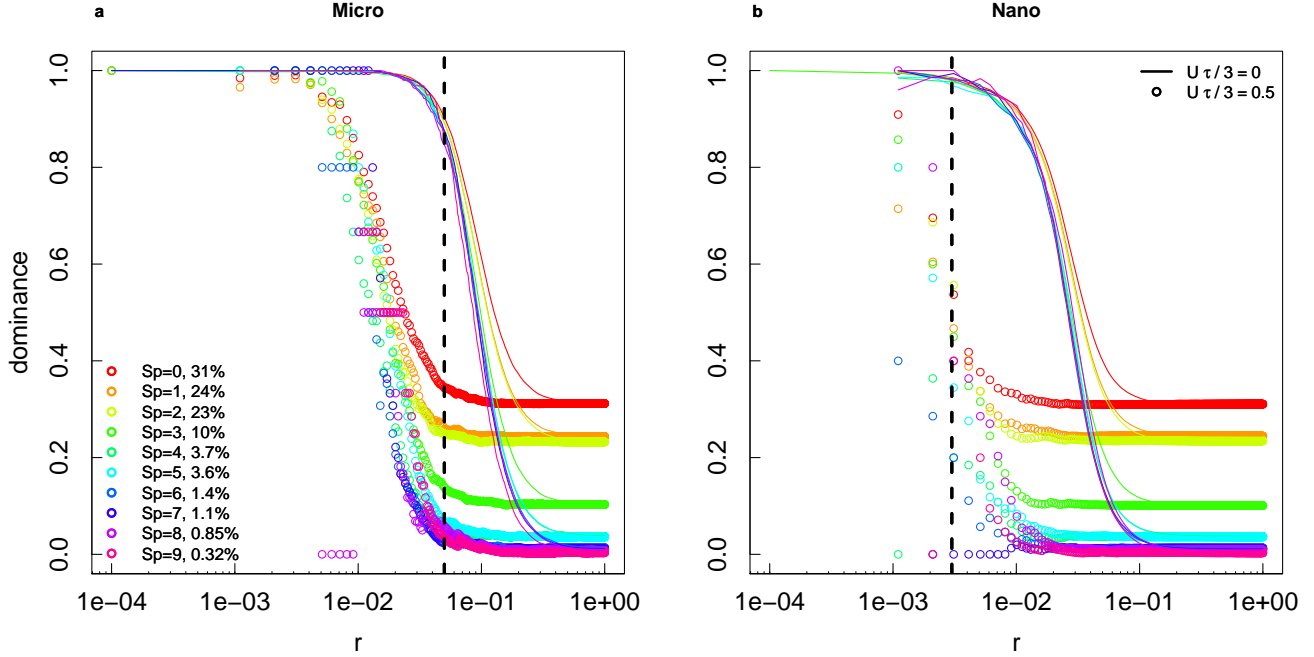


Figure 4: Dominance indices as a function of distance (in cm) for microphytoplankton (a) and nanophytoplankton (b) in a 10-species community with a skewed abundance distribution (final proportions in the community are indicated in the figure) after 1000 timesteps, with (circles) and without (lines) advection. Each color represents a different species. The black dashed line corresponds to the threshold considered as the maximum distance for nutrient-based competition.

Differences in spatial distributions are not only due to organism sizes, which determine their demographic and hydrodynamic properties, but also to their abundances (here set through initial values). In the presence of turbulence, the threshold distance at which dominance falls below 95% is smaller for more abundant species (Fig. 5 a-b). Abundant species tend to be present nearly everywhere when they are mixed in the environment. Therefore, they are also more likely to be close to a heterospecific, but still have more conspecifics close to them than the less abundant species ($\mathcal{D}(d_{\text{threshold}})$ increases with abundance, Fig. 5 c-d). However, this increase is less marked for nanophytoplankton than for microphytoplankton (Fig. 5 c-d). When turbulence is absent, the relationships with abundance are unclear, possibly affected by sampling effects, and we refrain from interpreting them.

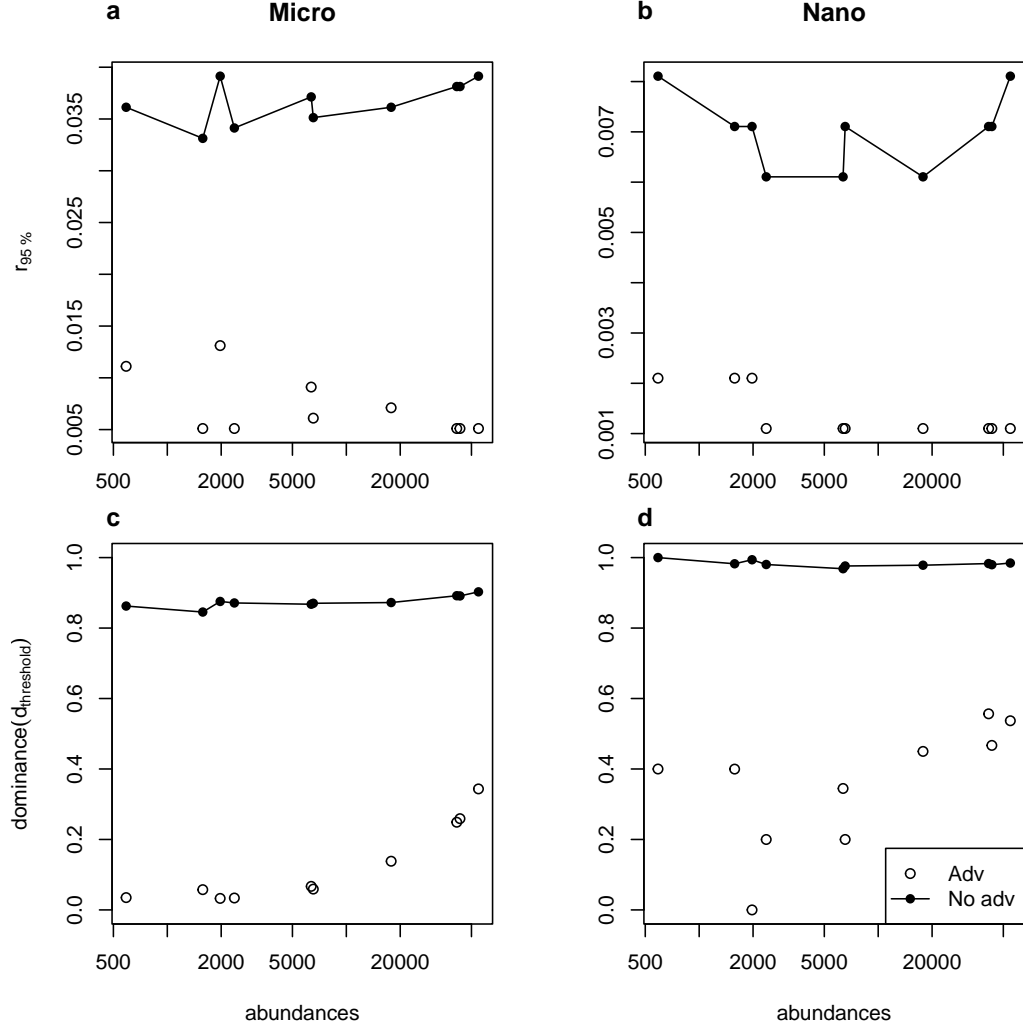


Figure 5: Minimum distances (in cm) between points for dominance to drop below 95% (a and b) and dominance at a distance corresponding to the threshold for competition (c and d) as a function of abundances (note the logarithmic scale on the x-axis) for microphytoplankton and nanophytoplankton. We consider cases with and without advection in a 10-species community with a skewed abundance distribution.

Discussion

We designed a stochastic, three-dimension, individual-based model of the spatial distribution of multiple species in a viscous and turbulent flow. We conducted both mathematical analyses and numerical simulations to quantify spatial correlations in organism distributions. We focused on the pair correlation function and Ripley's K -function, for which numerical and theoretical analyses showed a good agreement, and extracted a more ecologically-oriented metric from them, i.e. the dominance index. This statistic is the *local* average ratio of conspecifics, i.e., the number of organisms of the focal species in the neighbourhood of an individual of the same species, divided by the total number of organisms in that neighbourhood. Intraspecific clustering corresponds to a dominance index close to 1, which decreases when interspecific mixing increases. The choice of this index was motivated by two reasons: (1), it

is at its core a proportion of a focus species in a certain volume, i.e. a scale-dependent, localized metric bounded between 0 and 1 as opposed to other statistics whose values are less directly interpreted, and (2), it is easy to relate to coexistence theory as it describes the environment of an organism in terms of heterospecifics and conspecifics, which can, under certain hypotheses that we discuss below, be related to interspecific and intraspecific interactions. Comparing the distributions of organisms of different sizes, we showed that the presence and intensity (Section S7 of the SI) of turbulence always increased mixing, and that the species composition around an organism depended on its size, which mechanically determines its hydrodynamic properties (diffusivity), and is linked with its ecological characteristics (growth rate and density). Microphytoplankters (20 to 200 μm), larger cells with lower diffusivity, growth rate and abundance, were on average further away from other cells, due to their lower concentrations (Figure S10 of the SI), than nanophytoplankters (2 to 20 μm). However, they were surrounded by more heterospecifics than conspecifics within a volume of potential interactions, whose radius is defined as the maximum distance for which nutrient depletion volumes of two different individuals may overlap. If we consider that interactions between species (not modelled here), could occur with equal probability at all distances within the volume of potential interactions, we would conclude that microphytoplankters are more likely to interact with individuals from other species than with individuals of their own species. However, this affirmation is conditional upon interactions at 10 cell diameters from an individual being equally likely than at 1 diameter from an individual. If we keep in mind that interactions are more likely or stronger at very short distances, microphytoplankters may still experience more frequent effects of conspecifics than heterospecifics.

To see this, let us first focus on the smallest distances between organisms. The nearest neighbour of an organism was always an organism of the same species, and the minimum distance between conspecifics was always lower than expected for a uniform distribution (Section S6 of the SI). The dominance index remained close to 1 for distances below 10^{-2} cm or 10^{-3} cm for microphytoplankton and nanophytoplankton respectively. There was therefore always *some* intraspecific aggregation, i.e. conspecifics were always closer than heterospecifics at the lowest distances. This is due to the prevalence of demographic processes at individual scales, because an individual acts as a source point for other organisms of the same species, and hydrodynamic processes do not separate conspecifics fast enough to prevent aggregation. If we consider that interaction strengths are a smoothly decaying function of distance, a common assumption in spatial coexistence models (e.g., Bolker & Pacala, 1999; Law *et al.*, 2003), this implies that population-level intraspecific interactions could be stronger than interspecific interactions due to intraspecific micro-scale aggregation. However, the mechanisms of competition at this scale are poorly known, likely relying on multiple types of resources with different distributions in the environment, effects on the cell, uptakes, etc. Rather than weighting much more heavily the potential interactions with the closest neighbour(s) through an interaction kernel, we therefore chose conservatively to define a maximum distance for two organisms to possibly affect the concentrations of elements in the environment of each other. We consider that, at all distances below this threshold, interactions could happen between organisms. We continue the discussion with that simplification in mind, and

explicitly mention when it is relaxed.

Dominance indices began to decrease at distances above 10^{-3} cm, still below the maximum distance for interactions. At this distance and above, the balance between heterospecifics and conspecifics was much more sensitive to different phytoplankters' demographic and hydrodynamic traits. The species composition of an organism's neighbourhood depended on its size: nanophytoplankton organisms mainly shared their volume of potential interactions with conspecifics (the dominance index remained close to 1, even near the distance threshold, i.e. the maximum distance for the overlap of nutrient depletion volumes) while microphytoplankton organisms could affect both conspecifics and heterospecifics (the dominance index was often below 50% at the distance threshold, i.e. a particle's depletion zone probably overlapped with more heterospecifics' than conspecifics'). Microphytoplankters were therefore more likely to share their depletion volume with heterospecifics than nanophytoplankters. The rate of production of new microphytoplankton conspecifics was not sufficient to compensate for the mixing induced by turbulence and diffusivity, even though the diffusion range of microphytoplankters was smaller than that of nanophytoplankters. There may therefore be different mechanisms at play at the community level for microphytoplankton and nanophytoplankton to maintain coexistence. For nanophytoplankton, the spatial structure likely leads to more interactions between conspecifics than between heterospecifics. The distribution of microphytoplankton species, on the contrary, encourages more interactions between heterospecifics. If we consider that local interaction strengths are equal within the volume of potential interactions, scaling to the population level, we would likely observe stronger intra- over interspecific interactions for nanophytoplankton (a key factor in coexistence theory, Barabás *et al.*, 2017) but not necessarily so for microphytoplankton (however, see Section S8 in the SI, based on the Lotka-Volterra model).

All of the above discussion is based on a microphytoplankter's neighbourhood in its nutrient depletion volumes. To simplify the computation, we used maximum volumes of potential interactions, corresponding to a diffusive-only flow of nutrient particles. But when fluid turbulence increases, nutrient uptake increases, and the size of the depletion zone decreases (Karp-Boss *et al.*, 1996). The proportion of change in the depletion volume increases with the size of organism: a 10 μm -diameter organism might not experience any change, while the uptake of a 100 μm -diameter organism would increase by at least 50% (Karp-Boss *et al.*, 1996). Therefore the volume of potential interactions shrinks in the presence of turbulence for microphytoplankton, but not necessarily for nanophytoplankton. This is one additional reason why microphytoplankters might still be surrounded by conspecifics at ecologically meaningful distances and interacting more frequently with them.

Up to now, we have only focused on the dominance index, a localized proportion of conspecifics. However, interactions also depend on the absolute densities of individuals. Mechanically, when density decreases, the distances between neighbours increase, which explains that the distances between the low-abundance microphytoplankters tended to be greater than distances between the more abundant nanophytoplankters (Section S6 of the SI). Explicit mathematical models using pair densities to express interaction rates (e.g. Law *et al.*, 2003; Plank & Law, 2015)

may be able to incorporate those effects; however, as we highlight below, the timescales and spatial correlations that are seen in such models may not necessarily represent faithfully phytoplankton community dynamics.

Contrary to other similar models (e.g., Birch & Young, 2006; Bouderbala *et al.*, 2018), we did not consider explicit effects of local density on survival and fertility rates. Outside of simply maintaining analytical tractability, we had another, more biological reason to do so: we cannot be sure that these local density-dependencies make sense in our phytoplankton context. To understand why, consider that even if a species abundance is locally tripled, competition might not directly ensue at the time scales covered by our model, if nutrient depletion has not had time to set in yet. We would need lagged local density-dependencies, which are to our knowledge not leading to tractable spatial branching or dynamic point processes. We could, of course, directly model nutrients, perhaps as resource “points” with a dynamics of their own (Murrell, 2005; North & Ovaskainen, 2007), which in turn change the reproduction or death rate of individuals. If the resource points risk being depleted, this entails a negative spatial correlation between organisms and their resources (Murrell, 2005). And that is where such models might be inadequate. The phycosphere, a micro-environment at the periphery of a phytoplankton organism where communities of bacteria interact (Seymour *et al.*, 2017), can also impact phytoplankton fitness, both positively (cross-feeding) and negatively (algicidal activities of bacteria). This can sometimes lead to an accumulation of key resources close to the phytoplankter. This will lead to positive spatial correlations between consumers and their resources, and we currently do not have theoretical models to represent this (short of modelling precisely these bacteria).

Our model should be viewed as a first model of spatial distributions of multiple phytoplankton species in a realistic, three-dimensional environment at the microscale, describing only basic hydrodynamic and demographic processes. Using this model, we were able to guesstimate the differences in potential intra vs interspecific interactions between species, emerging at the population level through spatial distributions (Detto & Muller-Landau, 2016). It is worthwhile to keep in mind that there are numerous remaining features of phytoplankton physiology and life histories which we do not cover here, but may affect their spatial distributions. Many phytoplankters are able to move actively in three dimensions, which can favour cluster formation (Breier *et al.*, 2018). Even those who are believed to move passively actually often move along the vertical dimension by regulating their buoyancy (Reynolds, 2006), and can at times aggregate to form pairs (Font-Muñoz *et al.*, 2019). Finally, a part of spatial structure is explained by the partially colonial nature of microphytoplankton (Kiørboe *et al.*, 1990). This clearly calls for viewing our model as a null model to which more complex mechanistic models and their spatial outputs can be compared.

Declaration of Competing Interest

The authors declare that they have no known competing financial interests or personal relationships that could have appeared to influence the work reported in this paper.

Author contribution statement

Acknowledgments

FB and CP were supported by the grant ANR-20-CE45-0004. CP was supported by a PhD grant from the French Ministry of Research.

Appendices

Derivation of the spatial characteristics of the Brownian Bug Model

We show here how to compute the monospecific pair correlation function and Ripley's K -function of the Brownian Bug Model (see Young *et al.*, 2001 and Picoche *et al.*, 2022 for a detailed derivation of the master equation). As these formula only apply to intraspecies pairs, we ignore species' index in the following for the sake of clarity. Formula for standard processes are given in the Supplementary Information, for readers who want to familiarize with simpler models.

Proof of Eq. 4 and Eq. 5

In three dimensions, when the birth rate λ is the same as the mortality rate μ , the pair density $G(r)$ is a solution of

$$\frac{\partial G}{\partial t} = \frac{2D}{r^2} \frac{\partial}{\partial r} \left(r^2 \frac{\partial G}{\partial r} \right) + \frac{\gamma}{r^2} \frac{\partial}{\partial r} \left(r^4 \frac{\partial G}{\partial r} \right) + 2\lambda C \delta(\mathbf{r}). \quad (18)$$

Steady-state solution We first compute the steady-state solution, *i.e.*

$$\begin{aligned} 0 &= \frac{2D}{r^2} \frac{\partial}{\partial r} \left(r^2 \frac{\partial G}{\partial r} \right) + \frac{\gamma}{r^2} \frac{\partial}{\partial r} \left(r^4 \frac{\partial G}{\partial r} \right) + 2\lambda C \delta(\mathbf{r}) \\ 0 &= 4\pi r^2 \left(\frac{2D}{r^2} \frac{\partial}{\partial r} \left(r^2 \frac{\partial G}{\partial r} \right) + \frac{\gamma}{r^2} \frac{\partial}{\partial r} \left(r^4 \frac{\partial G}{\partial r} \right) + 2\lambda C \delta(\mathbf{r}) \right) \\ 0 &= 4\pi \left(2D \frac{\partial}{\partial r} \left(r^2 \frac{\partial G}{\partial r} \right) + \gamma \frac{\partial}{\partial r} \left(r^4 \frac{\partial G}{\partial r} \right) \right) + 4\pi r^2 2\lambda C \delta(\mathbf{r}). \end{aligned} \quad (19)$$

We can then integrate Eq. (18) over a small sphere centered on an individual, with radius ρ . Let us first note that

$$\begin{aligned} &\int_{\mathbb{R}^3} \delta(\mathbf{r}) d^3\mathbf{r} = 1 \\ \Leftrightarrow &\int_0^{2\pi} \int_0^\pi \int_0^\rho \delta(\mathbf{r}') r'^2 \sin(\phi) dr' d\phi d\theta = 1 \\ &\Leftrightarrow 4\pi \int_0^\rho \delta(\mathbf{r}') r'^2 dr' = 1. \end{aligned} \quad (20)$$

Using Eq. (19) and (20),

$$\begin{aligned} 0 &= 4\pi \left(2Dr^2 \frac{\partial G}{\partial r} + \gamma r^4 \frac{\partial G}{\partial r} \right) + 2\lambda C \\ \Leftrightarrow \frac{\partial G}{\partial r} &= -\frac{1}{4\pi} \frac{2\lambda C}{2Dr^2 + \gamma r^4}. \end{aligned} \quad (21)$$

We can integrate Eq. 21 between ρ and ∞ . As $G(\infty) = C^2$,

$$C^2 - G(\rho) = -\frac{\lambda C}{2\pi} \int_{\rho}^{\infty} \frac{1}{2Dr^2 + \gamma r^4} dr. \quad (22)$$

We first compute the primitive $A = \int \frac{1}{2Dr^2 + \gamma r^4} dr$.

$$A = \int \frac{1}{r^2(2D + \gamma r^2)} dr \quad (23)$$

$$= \int \frac{1}{2Dr^2} - \frac{\gamma}{2D(2D + \gamma r^2)} dr \quad (24)$$

$$= -\frac{1}{2Dr} - \frac{\gamma}{2D} \int \frac{1}{2D \left(1 + \left(\sqrt{\frac{\gamma}{2D}} r \right)^2 \right)} dr. \quad (25)$$

With a change of variable $u = \sqrt{\frac{\gamma}{2D}} r$, using $\int \frac{1}{1+u^2} = \arctan(u)$, we have

$$A = -\frac{1}{2Dr} - \frac{\sqrt{\gamma} \arctan\left(\frac{\sqrt{\gamma} r}{\sqrt{2D}}\right)}{2\sqrt{2D}\sqrt{D}} + K \quad (26)$$

where K is a constant. We can now compute $B = [A]_{\rho}^{\infty}$.

$$B = -\frac{\sqrt{\gamma}\pi}{4\sqrt{2D}\sqrt{D}} + \frac{1}{2D\rho} + \frac{\sqrt{\gamma} \arctan\left(\frac{\sqrt{\gamma}\rho}{\sqrt{2D}}\right)}{2\sqrt{2D}\sqrt{D}}. \quad (27)$$

This leads to

$$G(\rho) = C^2 + \frac{\lambda C}{2\pi} B \quad (28)$$

$$= C^2 + \frac{\lambda C}{2\pi} \left[\frac{1}{2D\rho} + \frac{\sqrt{\gamma} \arctan\left(\frac{\sqrt{\gamma}\rho}{\sqrt{2D}}\right)}{2\sqrt{2D}\sqrt{D}} - \frac{\sqrt{\gamma}\pi}{4\sqrt{2D}\sqrt{D}} \right]. \quad (29)$$

Finally, the pair correlation function $g = G/C^2$ is defined as

$$g(\rho) = \frac{\lambda}{4\pi CD} \left(\frac{\sqrt{\gamma} \arctan\left(\frac{\sqrt{\gamma}\rho}{\sqrt{2D}}\right)}{\sqrt{2D}} + \frac{1}{\rho} - \frac{\pi\sqrt{\gamma}}{2\sqrt{2D}} \right) + 1. \quad (30)$$

Time-dependent solution In the absence of advection by turbulent diffusion ($U = 0, \gamma = 0$), convergence to the steady-state solution can be very slow (more than a week, see Section S3 in the SI). In order to keep a realistic timeframe, we need to compute a time-dependent solution. We can get back to Eq. (18) with $\gamma = 0$, which yields

$$\frac{\partial G}{\partial t} = \frac{2D}{r^2} \frac{\partial}{\partial r} \left(r^2 \frac{\partial G}{\partial r} \right) + 2\lambda C \delta(\mathbf{r}). \quad (31)$$

Assuming an isotropic environment, this means

$$\frac{\partial G}{\partial t} - 2D\Delta G = 2\lambda C \delta(\mathbf{r}) \quad (32)$$

where $\Delta = \nabla^2$ is the Laplacian operator. We therefore have

$$\mathcal{L}G(\mathbf{r}, t) = 2\lambda C \delta(\mathbf{r}) \quad (33)$$

where \mathcal{L} is the linear differential operator $\partial_t - 2D\Delta$.

Using the Green's function theory, we know that $G(y) = \int H(y, s) 2\lambda C \delta(s) ds$ where $H(y, s) = H(y - s)$ is the Green kernel (heat kernel). We can therefore write

$$\begin{aligned} G(\mathbf{r}, t) &= 2\lambda C \int_{\mathbb{R}^3} \int_0^t H(\mathbf{r} - \mathbf{r}', t') \delta(\mathbf{r}') dr' dt' \\ \Leftrightarrow G(\mathbf{r}, t) &= 2\lambda C \int_0^t H(\mathbf{r}, t') dt'. \end{aligned} \quad (34)$$

A solution for the Green's function using $\mathcal{L} = \partial_t - 2D\Delta$ in 3 dimensions is $H(r, t) = \left(\frac{1}{8\pi Dt}\right)^{3/2} \exp\left(\frac{-r^2}{8Dt}\right)$. $G(r, t)$ can then be computed as

$$G(r, t) = 2\lambda C \left(\frac{-\operatorname{erf}\left(\frac{r}{\sqrt{8Dt}}\right)}{8\pi Dr} + K \right) \quad (35)$$

where erf is the error function. Using $G(r, 0) = C^2$ and $\lim_{x \rightarrow +\infty} \operatorname{erf}(x) = 1$ in Eq. (35),

$$\begin{aligned} C^2 &= 2\lambda C \left(\frac{1}{8\pi Dr} + K \right) \\ \Leftrightarrow \frac{C}{2\lambda} - \frac{1}{8\pi Dr} &= K. \end{aligned} \quad (36)$$

We can finally compute $G(r, t)$:

$$\begin{aligned} G(r, t) &= 2\lambda C \left(-\frac{\operatorname{erf}\left(\frac{r}{\sqrt{8Dt}}\right)}{8\pi Dr} + \frac{C}{2\lambda} + \frac{1}{8D\pi r} \right) \\ &= \frac{\lambda C}{4\pi Dr} \left\{ 1 - \operatorname{erf}\left(\frac{r}{\sqrt{8Dt}}\right) \right\} + C^2 \\ \Leftrightarrow g(r, t) &= \frac{\lambda}{4D\pi r C} \left\{ 1 - \operatorname{erf}\left(\frac{r}{\sqrt{8Dt}}\right) \right\} + 1. \end{aligned} \quad (37)$$

Proof of Eq. 8 and Eq. 9

We can integrate the pcf formula to compute Ripley's K -function, as $g(r) = \frac{K'(r)}{4\pi r^2}$.

Steady-state solution From Eq. 30,

$$K(\rho) = 4\pi \int_0^\rho r^2 + \frac{\lambda}{2\pi C} \left[\frac{r}{2D} + \frac{\sqrt{\gamma} r^2 \arctan\left(\frac{\sqrt{\gamma} r}{\sqrt{2D}}\right)}{2\sqrt{2D}\sqrt{D}} - \frac{\sqrt{\gamma} \pi r^2}{4\sqrt{2D}\sqrt{D}} \right] dr. \quad (38)$$

We define $A = \int_0^\rho r^2 dr$, $B = \int_0^\rho \frac{r}{2D} dr$, $C = \int_0^\rho r^2 \arctan\left(\frac{\sqrt{\gamma} r}{\sqrt{2D}}\right) dr$ and $E = \int_0^\rho \frac{\sqrt{\gamma} \pi r^2}{4\sqrt{2D}\sqrt{D}} dr$.

$$\begin{aligned} A &= \frac{1}{3} \rho^3. \\ B &= \frac{\rho^2}{4D}. \\ E &= \frac{\sqrt{\gamma} \pi \rho^3}{12\sqrt{2D}\sqrt{D}}. \end{aligned} \quad (39)$$

We can also compute $C = \int_0^\rho r^2 \arctan\left(\frac{\sqrt{\gamma} r}{\sqrt{2D}}\right) dr$. We first change variable, with $u = \frac{r}{\sqrt{2D}}$, $dr = \sqrt{2D} du$, and obtain

$$C = (2D)^{3/2} \int_0^{\rho/\sqrt{2D}} u^2 \arctan(\sqrt{\gamma} u) du. \quad (40)$$

We can integrate by parts, with $f = \arctan(\sqrt{\gamma} u)$ and $g' = u^2$, which leads to

$$C = (2D)^{3/2} \left(\frac{\rho^3}{3(2D)^{3/2}} \arctan(\sqrt{\frac{\gamma}{2D}} \rho) - \frac{\sqrt{\gamma}}{3} \int_0^{\rho/\sqrt{2D}} \frac{u^3}{(\gamma u^2 + 1)} du \right). \quad (41)$$

We then substitute $v = \gamma u^2 + 1$, $du = \frac{1}{2\gamma u} dv$, and have

$$\begin{aligned} \int_0^{\rho/\sqrt{2D}} \frac{u^3}{(\gamma u^2 + 1)} du &= \frac{1}{2\gamma^2} \int_1^{\gamma \rho^2/2D + 1} \frac{v-1}{v} dv \\ &= \frac{1}{2\gamma^2} \int_1^{\gamma \rho^2/2D + 1} 1 - \frac{1}{v} dv \\ &= \frac{1}{2\gamma^2} (\gamma \frac{\rho^2}{2D} - \log(\gamma \frac{\rho^2}{2D} + 1)). \end{aligned} \quad (42)$$

Going back to C , we obtain

$$\begin{aligned} C &= \frac{\rho^3 \arctan(\sqrt{\frac{\gamma}{2D}} \rho)}{3} - (2D)^{3/2} \frac{\sqrt{\gamma}}{3} \frac{1}{2\gamma^2} \left(\frac{\gamma}{2D} \rho^2 - \log(\gamma \frac{\rho^2}{2D} + 1) \right) \\ &= \frac{\rho^3 \arctan(\sqrt{\frac{\gamma}{2D}} \rho)}{3} - \frac{\sqrt{2D}}{6\sqrt{\gamma}} \rho^2 + \frac{\sqrt{2D}^{3/2}}{3\gamma^{3/2}} \log(\gamma \frac{\rho^2}{2D} + 1). \end{aligned} \quad (43)$$

Combining all equations,

$$\begin{aligned}
K(\rho) &= \frac{4}{3}\pi\rho^3 + \frac{2\lambda}{C} \left(\frac{\rho^2}{4D} + \frac{\sqrt{\gamma}\rho^3 \arctan(\sqrt{\frac{\gamma}{2D}}\rho)}{6\sqrt{2}D^{3/2}} - \frac{\rho^2}{12D} + \frac{\log(\gamma\frac{\rho^2}{2D}+1)}{6\gamma} - \frac{\sqrt{\gamma}\pi\rho^3}{12\sqrt{2}D\sqrt{D}} \right) \\
&= \frac{4}{3}\pi\rho^3 + \frac{\lambda}{3C} \left(\frac{\rho^2}{D} + \frac{\sqrt{\gamma}\rho^3 \arctan(\sqrt{\frac{\gamma}{2D}}\rho)}{\sqrt{2}D^{3/2}} + \frac{\log(\gamma\frac{\rho^2}{2D}+1)}{\gamma} - \frac{\sqrt{\gamma}\pi\rho^3}{2\sqrt{2}D\sqrt{D}} \right).
\end{aligned} \tag{44}$$

Note that in the absence of advection,

$$\begin{aligned}
g(r) &= \frac{\lambda}{4\pi CD r} + 1 \\
\Rightarrow K'(r) &= \frac{\lambda r}{CD} + 4\pi r^2 \\
\Leftrightarrow K(r) &= \frac{\lambda r^2}{2CD} + \frac{4}{3}\pi r^3.
\end{aligned} \tag{45}$$

Time-dependent solution In the absence of advection ($U = 0, \gamma = 0$), we need to compute a time-dependent solution. From eq. 37,

$$\begin{aligned}
K(\rho) &= \frac{\lambda}{CD} \int_0^\rho r \left\{ 1 - \operatorname{erf}\left(\frac{r}{\sqrt{8Dt}}\right) \right\} + 4\pi r^2 dr \\
&= \frac{\lambda}{CD} \left(\frac{\rho^2}{2} - \int_0^\rho r \times \operatorname{erf}\left(\frac{r}{\sqrt{8Dt}}\right) dr \right) + \frac{4}{3}\pi\rho^3.
\end{aligned} \tag{46}$$

We first compute the primitive for $\int_0^\rho r \times \operatorname{erf}\left(\frac{r}{\sqrt{8Dt}}\right) dr$. We define $u = \frac{r}{\sqrt{8Dt}}$, $dr = \sqrt{8Dt} du$, then

$$\int_0^\rho r \times \operatorname{erf}\left(\frac{r}{\sqrt{8Dt}}\right) dr = 8Dt \int_0^{\rho/\sqrt{8Dt}} u \times \operatorname{erf}(u) du. \tag{47}$$

We can integrate by parts, with $f = \operatorname{erf}(u)$ and $g' = u$, and obtain

$$8Dt \int_0^{\rho/\sqrt{8Dt}} u \times \operatorname{erf}(u) du = 8Dt \left(\frac{\rho^2}{2} \frac{1}{8Dt} \operatorname{erf}\left(\frac{\rho}{\sqrt{8Dt}}\right) - \frac{1}{\sqrt{\pi}} \int_0^{\rho/\sqrt{8Dt}} u^2 e^{-u^2} du \right). \tag{48}$$

We integrate by parts again, this time with $f = u$ and $g' = ue^{-u^2}$, which leads to

$$\int u^2 e^{-u^2} du = -\frac{ue^{-u^2}}{2} + \frac{1}{2} \int e^{-u^2} du = -\frac{ue^{-u^2}}{2} + \frac{\sqrt{\pi} \operatorname{erf}(u)}{4}. \tag{49}$$

If we use Eq. 49 in Eq. 48,

$$\begin{aligned}
8Dt \int_0^{\rho/\sqrt{8Dt}} u \times \operatorname{erf}(u) du &= 8Dt \left(\frac{\rho^2}{2} \frac{1}{8Dt} \operatorname{erf}\left(\frac{\rho}{\sqrt{8Dt}}\right) - \frac{\operatorname{erf}(\frac{\rho}{\sqrt{8Dt}})}{4} + \frac{1}{2\sqrt{\pi}} \frac{\rho}{\sqrt{8Dt}} e^{-\rho^2/8Dt} \right) \\
\Leftrightarrow \int_0^\rho r \times \operatorname{erf}\left(\frac{r}{\sqrt{8Dt}}\right) dr &= \frac{1}{2} \operatorname{erf}\left(\frac{\rho}{\sqrt{8Dt}}\right) (\rho^2 - 4Dt) + \frac{\sqrt{2Dt}}{\sqrt{\pi}} \rho e^{-\rho^2/8Dt}.
\end{aligned} \tag{50}$$

We can now compute $K(\rho)$:

$$K(\rho) = \frac{\lambda}{CD} \left(\frac{\rho^2}{2} - \frac{1}{2} \operatorname{erf}\left(\frac{\rho}{\sqrt{8Dt}}\right) (\rho^2 - 4Dt) - \frac{\sqrt{2Dt}\rho}{\sqrt{\pi}} e^{-\rho^2/8Dt} \right) + \frac{4}{3}\pi\rho^3. \tag{51}$$

References

- Adler, P.B., Smull, D., Beard, K.H., Choi, R.T., Furniss, T., Kulmatiski, A., Meiners, J.M., Tredennick, A.T. & Veblen, K.E. (2018). Competition and coexistence in plant communities: intraspecific competition is stronger than interspecific competition. *Ecology Letters*, 21, 1319–1329.
- Arnott, R.N., Cherif, M., Bryant, L.D. & Wain, D.J. (2021). Artificially generated turbulence: a review of phyco-logical nanocosm, microcosm, and mesocosm experiments. *Hydrobiologia*, 848, 961–991.
- Arrieta, J., Jeanneret, R., Roig, P. & Tuval, I. (2020). On the fate of sinking diatoms: the transport of active buoyancy-regulating cells in the ocean. *Philosophical Transactions of the Royal Society A*, 378, 20190529.
- Bainbridge, R. (1957). The size, shape and density of marine phytoplankton concentrations. *Biological Reviews*, 32, 91–115.
- Barabás, G., Michalska-Smith, M.J. & Allesina, S. (2017). Self-regulation and the stability of large ecological networks. *Nature Ecology & Evolution*, 1, 1870–1875.
- Barton, A.D., Ward, B.A., Williams, R.G. & Follows, M.J. (2014). The impact of fine-scale turbulence on phyto-plankton community structure. *Limnology and Oceanography: Fluids and Environments*, 4, 34–49.
- Bec, B., Collos, Y., Vaquer, A., Mouillot, D. & Souchu, P. (2008). Growth rate peaks at intermediate cell size in marine photosynthetic picoeukaryotes. *Limnology and Oceanography*, 53, 863–867.
- Benczik, I.J., Károlyi, G., Scheuring, I. & Tél, T. (2006). Coexistence of inertial competitors in chaotic flows. *Chaos*, 16, 043110.
- Birch, D.A. & Young, W.R. (2006). A master equation for a spatial population model with pair interactions. *Theoretical Population Biology*, 70, 26–42.
- Bissinger, J.E., Montagnes, D.J.S., Harples, J. & Atkinson, D. (2008). Predicting marine phytoplankton maxi-mum growth rates from temperature: improving on the Eppley curve using quantile regression. *Limnology and Oceanography*, 53, 487–493.
- Bolker, B.M. & Pacala, S.W. (1999). Spatial moment equations for plant competition: understanding spatial strategies and the advantages of short dispersal. *The American Naturalist*, 153, 575–602.
- Borgnino, M., Arrieta, J., Boffetta, G., De Lillo, F. & Tuval, I. (2019). Turbulence induces clustering and segregation of non-motile, buoyancy-regulating phytoplankton. *Journal of the Royal Society Interface*, 16, 20190324.
- Bouderbala, I., El Saadi, N., Bah, A. & Auger, P. (2018). A 3D individual-based model to study effects of chemotaxis, competition and diffusion on the motile-phytoplankton aggregation. *Acta Biotheoretica*, 66, 257–278.

- Breier, R.E., Lalescu, C.C., Waas, D., Wilczek, M. & Mazza, M.G. (2018). Emergence of phytoplankton patchiness at small scales in mild turbulence. *Proceedings of the National Academy of Sciences*, 115, 12112–12117.
- Chesson, P. (2018). Updates on mechanisms of maintenance of species diversity. *Journal of Ecology*, 106, 1773–1794.
- Detto, M. & Muller-Landau, H.C. (2016). Stabilization of species coexistence in spatial models through the aggregation-segregation effect generated by local dispersal and nonspecific local interactions. *Theoretical Population Biology*, 112, 97–108.
- Doubell, M.J., Seuront, L., Seymour, J.R., Patten, N.L. & Mitchell, J.G. (2006). High-resolution fluorometer for mapping microscale phytoplankton distributions. *Applied and Environmental Microbiology*, 72, 4475–4478.
- Dusenbery, D. (2009). *Living at the microscale*. Harvard University Press.
- Edwards, K.F. (2019). Mixotrophy in nanoflagellates across environmental gradients in the ocean. *Proceedings of the National Academy of Sciences*, p. 201814860.
- Einstein, A. (1905). Über die von der molekularkinetischen theorie der wärme geforderte bewegung von in ruhenden flüssigkeiten suspendierten teilchen. *Annalen der physik*, 4.
- Estrada, M., Alcaraz, M. & Marrasé, C. (1987). Effects of turbulence on the composition of phytoplankton assemblages in marine microcosms. *Marine Ecology Progress Series*, 38, 267–281.
- Field, C.B., Behrenfeld, M.J., Randerson, J.T. & Falkowski, P. (1998). Primary production of the biosphere: integrating terrestrial and oceanic components. *Science*, 281, 237–240.
- Font-Muñoz, J.S., Jeanneret, R., Arrieta, J., Anglès, S., Jordi, A., Tuval, I. & Basterretxea, G. (2019). Collective sinking promotes selective cell pairing in planktonic pennate diatoms. *Proceedings of the National Academy of Sciences*, 116, 15997–16002.
- Font-Muñoz, J.S., Jordi, A., Tuval, I., Arrieta, J., Anglès, S. & Basterretxea, G. (2017). Advection by ocean currents modifies phytoplankton size structure. *Journal of the Royal Society Interface*, 14, 20170046.
- Hellweger, F.L. & Bucci, V. (2009). A bunch of tiny individuals – individual-based modeling for microbes. *Ecological Modelling*, 220, 8–22.
- Huisman, J. & Weissing, F.J. (1999). Biodiversity of plankton by species oscillations and chaos. *Nature*, 402, 407–410.
- Hutchinson, G.E. (1961). The paradox of the plankton. *The American Naturalist*, 95, 137–145.
- Illian, J., Penttinen, A., Stoyan, H. & Stoyan, D. (2008). *Statistical analysis and modelling of spatial point patterns*. vol. 70. John Wiley & Sons.

- Jumars, P.A., Deming, J., Hill, P., Karp-Boss, L., Yager, P. & Dade, W. (1993). Physical constraints on marine osmotrophy in an optimal foraging context. *Marine Microbial Food Webs*, 7, 121–159.
- Karp-Boss, L., Boss, E. & Jumars, P.A. (1996). Nutrient fluxes to planktonic osmotrophs in the presence of fluid motion. *Oceanography and Marine Biology: An Annual Review*, 34, 71–107.
- Kjørboe, T., Andersen, K.P. & Dam, H.G. (1990). Coagulation efficiency and aggregate formation in marine phytoplankton. *Marine Biology*, 107, 235–245.
- Law, R., Murrell, D.J. & Dieckmann, U. (2003). Population growth in space and time: spatial logistic equations. *Ecology*, 84, 252–262.
- Leonard, C.L., Bidigare, R.R., Seki, M.P. & Polovina, J.J. (2001). Interannual mesoscale physical and biological variability in the North Pacific Central Gyre. *Progress in Oceanography*, 49, 227–244.
- Levine, J.M. & HilleRisLambers, J. (2009). The importance of niches for the maintenance of species diversity. *Nature*, 461, 254–257.
- Li, L. & Chesson, P. (2016). The effects of dynamical rates on species coexistence in a variable environment: the paradox of the plankton revisited. *The American Naturalist*, 188, E46–E58.
- MacArthur, R. & Levins, R. (1964). Competition, habitat selection and character displacement in a patchy environment. *Proceedings of the National Academy of Sciences*, 51, 1207–1210.
- Martin, A.P. (2003). Phytoplankton patchiness: the role of lateral stirring and mixing. *Progress in Oceanography*, 57, 125–174.
- Murrell, D. (2005). Local spatial structure and predator-prey dynamics: counterintuitive effects of prey enrichment. *The American Naturalist*, 166, 354–367.
- Ngan, K. & Vanneste, J. (2011). Scalar decay in a three-dimensional chaotic flow. *Physical Review E*, 83, 056306.
- North, A. & Ovaskainen, O. (2007). Interactions between dispersal, competition, and landscape heterogeneity. *Oikos*, 116, 1106–1119.
- Peters, F. & Marrasé, C. (2000). Effects of turbulence on plankton: an overview of experimental evidence and some theoretical considerations. *Marine Ecology Progress Series*, 205, 291–306.
- Picoche, C. & Barraquand, F. (2019). How self-regulation, the storage effect, and their interaction contribute to coexistence in stochastic and seasonal environments. *Theor Ecol*, 12, 489–500.
- Picoche, C. & Barraquand, F. (2020). Strong self-regulation and widespread facilitative interactions in phytoplankton communities. *Journal of Ecology*, 108, 2232–2242.

- Picoche, C., Young, W.R. & Barraquand, F. (2022). [Re] Reproductive pair correlations and the clustering of organisms. *ReScience C*, 8.
- Pierrehumbert, R.T. (1994). Tracer microstructure in the large-eddy dominated regime. *Chaos, Solitons & Fractals*, 4, 1091–1110.
- Plank, M.J. & Law, R. (2015). Spatial point processes and moment dynamics in the life sciences: a parsimonious derivation and some extensions. *Bulletin of Mathematical Biology*, 77, 586–613.
- Prairie, J.C., Sutherland, K.R., Nickols, K.J. & Kaltenberg, A.M. (2012). Biophysical interactions in the plankton: a cross-scale review. *Limnology and Oceanography: Fluids and Environments*, 2, 121–145.
- Record, N.R., Pershing, A.J. & Maps, F. (2014). The paradox of the “paradox of the plankton”. *ICES Journal of Marine Science*, 71, 236–240.
- REPHY (2017). *REPHY dataset - French Observation and Monitoring program for Phytoplankton and Hydrology in coastal waters. 1987-2016 Metropolitan data*. <https://www.seanoe.org/data/00361/47248/>.
- Reynolds, C.S. (2006). *The ecology of phytoplankton*. Cambridge University Press.
- Schippers, P., Verschoor, A.M., Vos, M. & Mooij, W.M. (2001). Does “supersaturated coexistence” resolve the “paradox of the plankton”? *Ecology Letters*, 4, 404–407.
- Seymour, J.R., Amin, S.A., Raina, J.B. & Stocker, R. (2017). Zooming in on the phycosphere: the ecological interface for phytoplankton–bacteria relationships. *Nature Microbiology*, 2, 17065.
- Stocker, R. (2012). Marine microbes see a sea of gradients. *Science*, 338, 628–633.
- Widdicombe, C. & Harbour, D. (2021). Phytoplankton taxonomic abundance and biomass time-series at Plymouth Station L4 in the Western English Channel, 1992-2020.
- Wiegand, T., Gunatilleke, C.V.S., Gunatilleke, I.A.U.N. & Huth, A. (2007). How individual species structure diversity in tropical forests. *Proceedings of the National Academy of Sciences*, 104, 19029–19033.
- Young, W.R., Roberts, A.J. & Stuhne, G. (2001). Reproductive pair correlations and the clustering of organisms. *Nature*, 412, 328–331.